JOURNAL OF MATERIALS SCIENCE 29 (1994) 5005–5013

Solidification morphology and semi-solid deformation in superalloy Rene 108

Part IV *Directionally solidified microstructures*

C. S. LIN, J. A. SEKHAR
Department of Materials Science and Engineering, International Center for Micropyretics, University of Cincinnati, Cincinnati, OH 45221-0012, USA

A high temperature nickel-base superalloy (Rene 108) was directionally solidified by imposing various growth rates and thermal gradients using a modified Bridgeman apparatus. The scaling of the solidification structure was recorded as a function of the imposed growth variables. A special Gleeble testing procedure, developed previously where the solidified samples were quickly raised to a predetermined temperature in the semi-solid zone and fractured, was used for the measurement of fracture conditions in the semi-solid region. The effect of the solidification process variables, namely, the temperature gradient and velocity, on the fracture stress in the transverse direction was to increase the fracture stress at a given temperature. The upper hot-tearing temperature was noted to be a function of the solidification variables. The amount of strain accommodation and the hot tearing resistance was found to be influenced by the solidification microstructure. Fracture maps, which include the temperature, transverse fracture stress and temperature gradient during solidification (T–σ_T–G), for the directionally solidified microstructures are presented. Castability maps are created from the microstructure and the fracture data and display the porosity and semi-solid strength as a function of the casting variables.

1. Introduction

Directional solidification technology has been applied successfully to the production of columnar and single-crystal turbine blades from superalloys. It is known that the solidification conditions influence the final properties of superalloy [1–5] through the microstructure and the defects and cracks generated during solidification. Demanding processing conditions are being imposed on superalloys to create complex parts such as integral rotors. The influence of the processing parameters on castability is therefore required to be critically understood. The influence of the primary and secondary scales of microstructures on the mechanical properties in the mushy zone during solidification of nickel aluminides has recently been studied [2, 3]. Unfortunately, there are no such studies available for the semi-solid deformation characteristics of nickel-base alloys. Such studies are expected to yield valuable guidelines for the processing of superalloys and for determining the conditions for hot-tearing and residual defects in critically processed castings. Although hot-tearing in directionally solidified structures is not as severe a problem as hot-tearing in equiaxed structures, examples exist where hot-tearing has been known to limit the processing of alloys during directional solidification, especially when section size issues become important. In addition, a positive temperature gradient is always present during directional solidification which may impose thermal stresses during solidification. Such stresses may be the cause of residual microcracks in the cast part. A knowledge of the properties of the semi-solid mass are thus important for determining the proper processing parameters during casting and for the design of an adequate mould. The purpose of the present investigation was to study the high temperature mechanical properties of a directionally solidified nickel-base superalloy, Rene 108, to obtain information on the mechanism of deformation characteristics in the semi-solid region. The nominal composition for Rene 108 is given in Table I. In this paper the influence of the solidification morphology on the mechanical properties of the mushy zone is reported. In addition, the solidification microstructure scales for Rene 108 are compared with the available data for other superalloys, and with the published theoretical models for the prediction of such microstructures.

2. Experimental procedure

The directional solidification experiments were conducted utilizing a modified Bridgeman technique (see Fig. 1). Each specimen was inductively melted and unidirectionally solidified in a high purity alumina tube (6.0 mm inner diameter × 2.0 mm thickness × 20.5 cm height) under an argon atmosphere. Induction melting

0022–2461

TABLE I Compositions in weight per cent of alloys have been studied [3, 4]. The alloy considered for the present study is Rene 108

Alloy	Ni	Co	Cr	Al	Ti	C	Ta	Mo	W	Nb	Zr	B	Hf
MAR-M 246	Bal.	10.0	9.0	5.5	1.5	0.15	1.5	2.5	10.0	–	0.05	0.015	–
IN 738LC	Bal.	8.5	16	3.5	3.5	0.11	1.6	1.75	2.5	0.7	0.08	0.008	–
IN 713C	Bal.	–	12.5	6.1	0.8	0.12	–	4.2	–	2.0	0.1	0.012	–
IC 50	Bal.	–	–	11.3	–	–	–	–	–	–	0.6	0.02	–
IC 396M	Bal.	–	7.72	7.98	–	–	–	3.02	–	–	0.85	0.005	–
Rene 108	Bal.	9.48	8.31	5.45	0.72	0.08	2.99	0.47	9.44	–	0.01	–	1.48

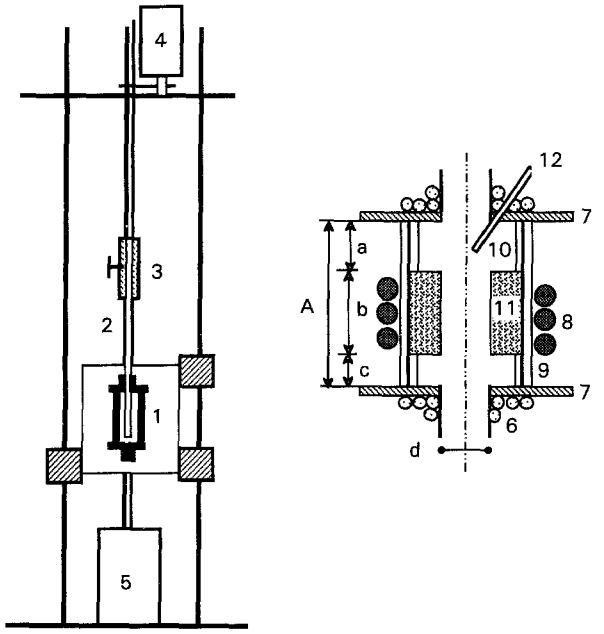

Figure 1 Schematic design of the experimental system (left) and the detailed view of the solidification cell. (1) Temperature gradient assembly, (2) ceramic tube with Rene 108 sample, (3) fixture, (4) compumotor, (5) quenching container, (6) water cooler, (7) lower and upper copper plate, (8) induction coil, (9) outer Al_2O_3 tube, (10) inner Al_2O_3 tube, (11) graphite tube, (12) Argon inlet.

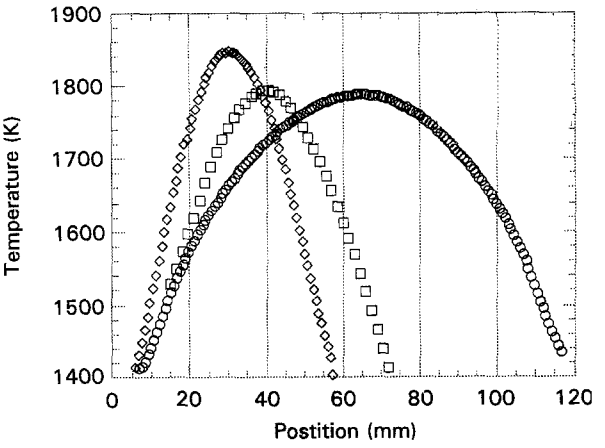

Figure 2 Temperature profiles measured inside the three solidification cells at a vertical velocity (upwards) of $V = 75\ \mu m\,s^{-1}$ with the optical fibre thermometer (OFT) system. (○) Assembly 1, (□) Assembly 2, (◇) Assembly 3.

TABLE II Mean temperature gradients in the mushy zone, G_M, and the temperature gradient at the liquidus temperature, G_L

	G_M (K mm^{-1})	G_L (K mm^{-1})
Assembly 1	8.1	4.2
Assembly 2	13.6	9.5
Assembly 3	23.8	17.1

was accomplished using a 30 kW power supply with a frequency of 450 kHz. The alumina tubes were embedded in a graphite susceptor in order to provide efficient heating. The temperature was measured by an optical fibre thermometer (OFT) (Accufiber model 100c). Temperature profiles were determined with a traversing molybdenum cylinder [2, 3]. The molybdenum cylinder was closed at one end, thus forming a black body into which a lightpipe was inserted. A sapphire protection tube isolated the lightpipe from the molybdenum walls (contactless temperature measurement). A data acquisition unit translated the radiation intensity into temperature values. The resolution of the lightpipe was 0.01 K. The data was directly transmitted from the OFT-system to a Macintosh computer by a standard RS-232 cable. For the experiments, by examining a quenched interface and establishing its flatness, it was ensured that there was no transverse temperature gradient in the alumina tube and the graphite susceptor during directional solidification. Three temperature gradient assemblies were used. Fig. 2 shows the temperature profiles of the three assemblies. The mean temperature gradient in the mush zone, G_M, was determined between liquidus temperature (1769 K) and the solidus temperature (1400 K). The temperature gradient at the liquidus temperature, G_L, was also measured and is given in Table II. The three temperature gradients used in the study were 8.1, 13.6 and 23.8 K mm^{-1}.

The specimen withdrawal rate was controlled using a linear motor (Parker Computor model 2100). In the present study, the growth rate, V, was assumed to be equal to the withdrawal rate of the crucible. The growth rates used ranged between 4.7 and 150 $\mu m\,s^{-1}$. Under these thermal conditions the solidification morphology was observed to change from two-fold cellular to dendritic morphology. Two-fold cellular morphologies were previously recorded for nickel aluminides [4]. Typical micrographs of the cellular and dendritic morphologies obtained are shown in Fig. 3.

Metallographic studies were conducted on as-quenched samples following directional solidification. The directionally solidified samples were cut both longitudinally (i.e. parallel to heat flow) and transversely (i.e. perpendicular to heat flow). Cut sections of the samples were etched with a solution of 4HCl, $3HNO_3$, 2glacial acetic acid, 1glycerol. Photomicrographs at magnifications of $\times$ 50–500 were taken to reveal different scales of the microstructure, e.g. the primary dendrite arm spacing and the secondary dendrite arm

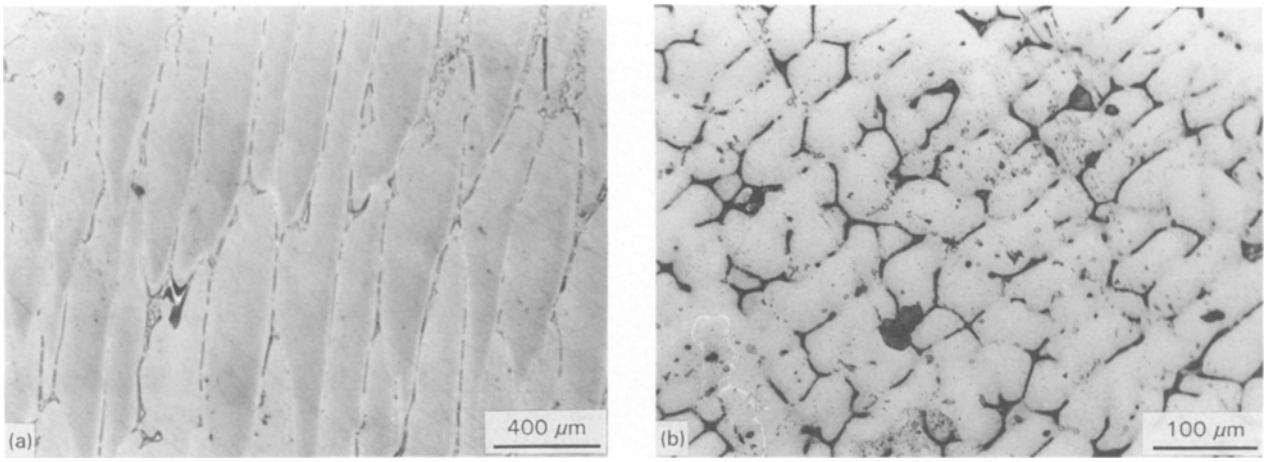

Figure 3 Optical micrograph showing the effect of growth rate on the longitudinal microstructure of directionally solidified Rene 108 at a temperature gradient of 8.1 K mm^{-1} at two growth rates: (a) 4.7 μm s^{-1} (cellular); (b) 150 μm s^{-1} (dendritic).

spacing were measured at × 100 and × 200 respectively, whereas microporosity measurements were taken at × 500. Primary γ′ measurements were taken at × 500. The use of an image analysis system, in combination with high magnification micrographs, provided accurate, reproducible measurements of the microstructural characteristics of interest. The strength in the semi-solid zone was measured with a Gleeble unit (a thermomechanical testing device manufactured by the Duffers Scientific, Inc.) as discussed in our previous articles [2, 3]. Samples of Rene 108 grown under different conditions were cut both longitudinally (i.e. parallel to heat flow) and transversely (i.e. perpendicular to heat flow).

Gleeble testing of the Rene 108 samples (with water cooled ends for gripping) was performed at various temperatures with an argon cover. The local temperature along the fracture line was measured with a K-type thermocouple which was spot welded to the specimen. Continuous temperature recording was made during the test.

3. Experimental results

Experiments were carried out with the Rene 108 alloy over a wide range of growth rates for three different temperature gradients. The experimental conditions used in the present study are summarized in Table III.

3.1. Primary arm spacing

The primary arm spacing, for both dendrites and cells, decreased monotonically with the growth rate; one example is shown in Fig. 4. Furthermore, the results from Fig. 4 also show that the primary arm spacing decreased proportionally with growth rate to a power of 0.2. This observation is in good agreement with the results of Ho *et al.* [4] and Kim *et al.* [6] for Ni_3Al, and Bolling and Fainstein-Pedraza [7] for Fe–Ni alloys.

3.2. Secondary dendrite arm spacing

A plot of secondary dendrite arm spacing (λ_2) versus growth rate is shown in Fig. 4. The results indicate a monotonic decrease in λ_2 with increasing growth rate. The results also show that the λ_2 decreased proportionally with growth rate to a power of 0.46.

TABLE III Directional solidification experiments on Rene 108

Gradient (K mm^{-1})	Velocity (μm s^{-1})	Microstructure	λ_1 (μm)	λ_2 (μm)
8.1	4.7	Cell	275	–
8.1	19	Dendrite	256	84
8.1	37	Dendrite	257	65
8.1	75	Dendrite	182	48
8.1	150	Dendrite	130	32
13.6	9	Cell	114	–
13.6	19	Dendrite	130	48
13.6	37	Dendrite	115	37
23.8	4.7	Cell	99	–
23.8	75	Dendrite	96	42
23.8	150	Dendrite	60	23

3.3. Microstructure and porosity

The mechanism for microporosity formation during the directional solidification process is attributed to the shrinkage of the ordered γ′ phase during liquid/solid transformation in the interdendritic region [4]. The γ′ formed behind the tip of the primary dendrite and, in the case of dendrite formation, only on the tip of a secondary arm growing some distance behind the primary tip. All of the microporosity was concentrated at the tips of the γ′ cells. The variations in volume fraction of γ′ and porosity (V_p) for nickel-base Rene 108 were measured and plotted versus the imposed growth condition and imposed temperature gradients, as shown in Fig. 5. Note that V_p and the volume fraction of γ′ increased with increasing velocity. However, both these values showed a minimum and maximum at an intermediate temperature gradient.

3.4. Stress–strain relationship in the semi-solid zone

The stress–strain relationships for Rene 108 were obtained with the Gleeble at the various temperatures

TABLE IV Measured mushy zone properties from stress free directionally solidified Rene 108

G (K mm^{-1})	V (μm s^{-1})	Temperature (K)	σ_f (MPa)	E_T (MPa)
8.1	4.7	1362	115.8	2617.6
8.1	4.7	1372	15.989	137.49
8.1	4.7	1459	2.014	402.80
8.1	37	1411	45.508	1190.9
8.1	37	1415	41.491	289.89
8.1	37	1430	5.6380	296.74
8.1	37	1445	5.1850	982.00
8.1	75	1378	94.929	3604.2
8.1	75	1407	48.925	2111.8
8.1	75	1447	33.666	486.22
8.1	75	1473	1.2450	177.86
8.1	150	1399	146.47	3035.4
8.1	150	1416	138.05	2975.3
8.1	150	1438	55.388	1429.5
8.1	150	1453	40.269	2202.6
13.6	9	1352	64.361	4527.9
13.6	9	1389	60.496	2787.9
13.6	9	1431	31.169	2630.8
13.6	9	1450	15.989	227.03
13.6	37	1354	112.00	1223.0
13.6	37	1457	11.516	2667.0
13.6	37	1458	9.0700	213.50
13.6	37	1461	0.9660	2.8182
23.8	75	1389	90.909	5760.2
23.8	75	1410	61.979	4598.2
23.8	75	1472	13.615	1844.1
23.8	75	1476	8.677	696.92

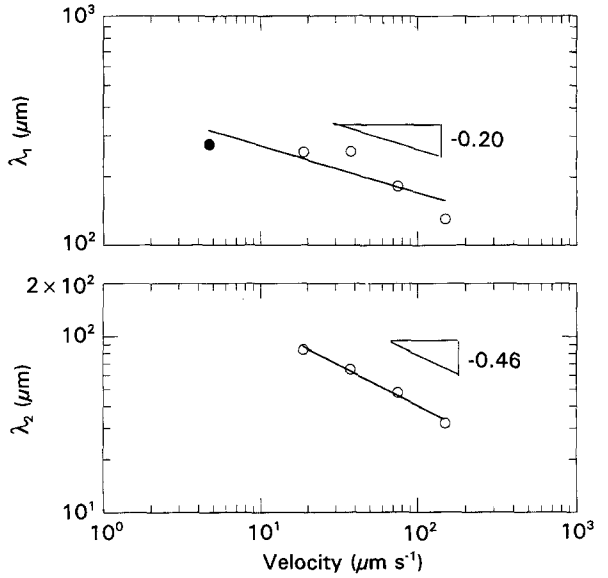

Figure 4 Variation in primary arm spacing (λ_1) and the secondary dendrite arm spacing (λ_2) with growth rate for temperature gradient, G = 8.1 K mm^{-1}. (●) Cellular, (○) dendrite.

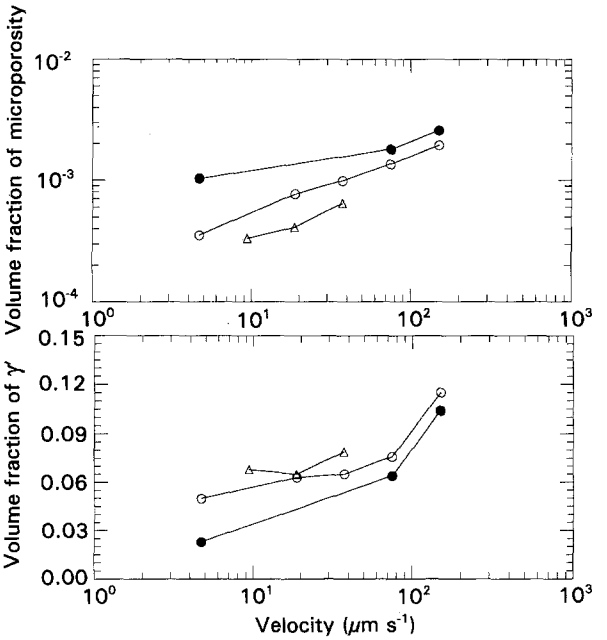

Figure 5 Variation of the volume fraction intrinsic porosity (V_p) and γ' with velocity for different gradients. (—○—) G = 8.1 K mm^{-1}, (—△—) G = 13.6 K mm^{-1}, (—●—) G = 23.8 K mm^{-1}.

between 1362 and 1473 K for the directionally solidified microstructures. In these experiments, the onset of the liquid phase at the intercellular boundary at ca. 1400 K was noted. However, the only other information on Rene 108 [8] shows that the liquid phase is noted only at 1705 K. For the work reported in this study 1400 K was taken as the solidus temperature. A typical stress–strain relationship is shown in Fig. 6. Table IV shows the measured modulus as a function of the temperature and solidification variables for the samples tested in this study. The measurement of the modulus was carried out in a manner similar to that described in Refs [2 and 3].

4. Discussion

4.1. Growth morphology

As noted above, three kinds of morphologies (cells, dendrites and two-fold dendrites) were observed in the present investigation. In order to provide insight into

TABLE V Summary of experimentally determined solidification parameters for front solidification of nickel-base superalloys compared to the present experimental data

Alloy	G (K mm^{-1})	V_c (mm s^{-1})	G/V_c (K s mm^{-1})	ΔT_0 (K)	$D_L = \Delta T_0(G/V_c)^{-1}$ (mm^2 s^{-1})	Reference
MAR-M 002	20	$< 1.67 \times 10^{-3}$	1.2×10^4	ca. 100	ca. 8.3×10^{-3}	[3]
MAR-M 200	10	1.0×10^{-3}	1×10^4	139	13.9×10^{-3}	[3]
MAR-M 246	20	$< 1.67 \times 10^{-3}$	1.2×10^4	ca. 100	ca. 8.3×10^{-3}	[3]
IN 738LC	20	$< 1.67 \times 10^{-3}$	1.2×10^4	85	7.1×10^{-3}	[3]
IN 713C	11	0.83×10^{-3}	1.3×10^4	30	2.3×10^{-3}	[3]
IC 50	5.44	$> 2.7 \times 10^{-3}$	$> 2.2 \times 10^3$	11	5.0×10^{-3}	[4]
Rene 108	8.1	$< 4.69 \times 10^{-3}$	$> 1.72 \times 10^3$	369	$< 214 \times 10^{-3}$	Present work
	13.6	$< 9.39 \times 10^{-3}$	$> 1.44 \times 10^3$	369	$< 256 \times 10^{-3}$	Present work
	23.8	$< 4.69 \times 10^{-3}$	$> 5.07 \times 10^3$	369	$< 72 \times 10^{-3}$	Present work

G, temperature gradient; V_c, planar break-up velocity; ΔT_0, alloy freezing range; D_L, solute diffusivity in the liquid alloy.

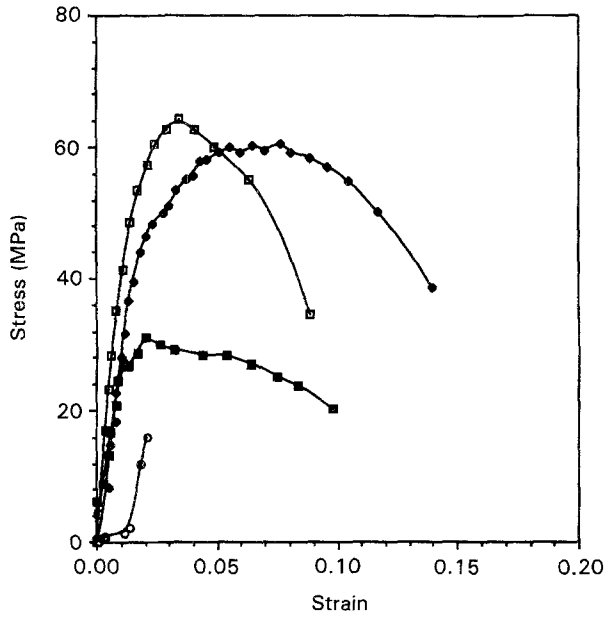

Figure 6 Stress–strain relationship for directionally solidified microstructure, $G = 13.6$ K mm^{-1}, $V = 9$ μm s^{-1}. (⊡) 1352 K, (◆) 1425 K, (■) 1445 K, (○) 1450 K.

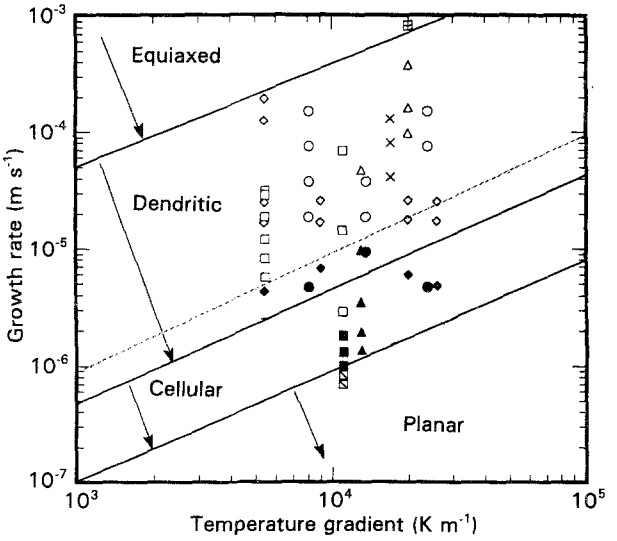

Figure 7 Plot showing the different solidification morphologies obtained under various combinations of growth rate and temperature gradient for nickel base superalloys [6] and Ni_3Al [4, 5]. The data points for Rene 108 are the present experimental results. The dashed line represents the cellular–dendritic transition for Rene 108. ○ Rene 108 d; ● Rene 108 c; ◇ IC396M d; ◆ IC396M c; ⊡ IC50 d; - IC50 c; □ IN713C d; ■ IN713C c; ⧅ IN713C p; △ MARM246 d; ▲ MARM246 c; × IN738LC d; + IN738LC c; ⊞ IN738LC e; p: planar; c: cellular; d: dendritic; e: equiaxed.

the experimental results the data were compared with results from other investigations, shown in Fig. 6. IC 50 [6] and IC 396M [4] are nickel–aluminide intermetallic compounds, and IN 713C, IN 738LC and MAR-M 246 are nickel-base superalloys of various compositions [5]. Solidification conditions are given in Table V.

4.2. Primary arm spacing (λ_1)

Although the cellular dendrite transition velocity may depend on dynamical effects, Kurz and Fisher [9] have suggested a simplified criterion where, for $V > V_c/k$, the microstructure would be dendritic, whereas for $V < V_c/k$ it would be cellular. V_c is the planar break up velocity $= GD/\Delta T_0$ (G, D and ΔT_0 are the temperature gradient, solute diffusivity and alloy freezing range, respectively). This suggestion was subsequently verified for a number of alloy systems [10, 11]. The critical growth rate at which the cellular–dendrite transition should occur may be calculated by assuming $k = 0.1$, $\Delta T_0 = 369$ K, $D = 13.9 \times 10^{-9}$ m^2 s^{-1} and the experimental conditions shown in Table IV. The cellular–dendrite transition should be observed at a growth rate of 3 μm s^{-1} for $G = 8.1$ K mm^{-1}, 5 μm s^{-1} range for $G = 13.6$ K mm^{-1} and 9 μm s^{-1} range for $G = 23.8$ K mm^{-1}. The experimental results for the present investigation suggest the transition growth rate occurred in the 4.7–18.8 μm s^{-1} range for $G = 8.1$ K mm^{-1}, 9.9–18.8 μm s^{-1} range for $G = 13.6$ K mm^{-1} and 4.7–37.5 μm s^{-1} range for $G = 23.8$ K mm^{-1} (see Fig. 7). The transition velocity shown in Fig. 7 is important for the castability maps.

For the changes in λ_1 with growth conditions, recent theoretical analysis by Burden and Hunt [12, 13] and Kurz and Fisher [9] show a relationship of the form:

$$\lambda_1 = KG^{-0.5}V^{-0.25} \quad (1)$$

where the value of K includes compositional dependence. The results of the present study, calculated using Equation 1, are shown in Fig. 8. The results in Fig. 8 show that all the data points fell on a straight line,

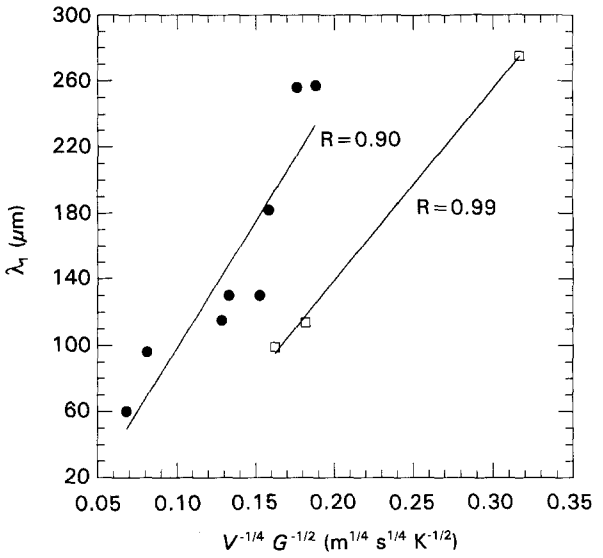

Figure 8 Variations in the value of the primary cell or dendrite arm spacing λ_1 plotted as a function of $V^{-1/4}\,G^{-1/2}$ for the directionally solidified nickel-base superalloy Rene 108. (—●—) Dendritic, (—⊟—) Cellular.

indicating good agreement with the results calculated from Equation 1. Esheiman *et al.* [14] and Kurz and Fisher [9] have shown that the spacing increases as the growth rate is increased across the cell dendrite transition. The value of K (Equation 1) is calculated to be $1.83 \times 10^3\ m^{3/4}\,s^{-1/4}\,K^{1/2}$ for the cells and $1.78 \times 10^3\ m^{3/4}\,s^{-1/4}\,K^{1/2}$ for the dendrite.

4.3. Secondary dendrite arm spacing

For the case of directional solidification, the local solidification time is given by:

$$t_f = \frac{\Delta T'}{|\dot{T}|} = \frac{\Delta T_0}{|GV|} \qquad (2)$$

where $\Delta T'$ = dendrite tip-to-root temperature difference and ΔT_0 = liquidus–solidus alloy freezing range at Co. Assuming $\Delta T' = \Delta T_0 = 369$ K [8], the local solidification time can be calculated. From the values of λ_2 and t_f, the exponent was calculated to be 0.28. This observation is in good agreement with the models of Flemings [15] and Feurer and Wunderlin [16].

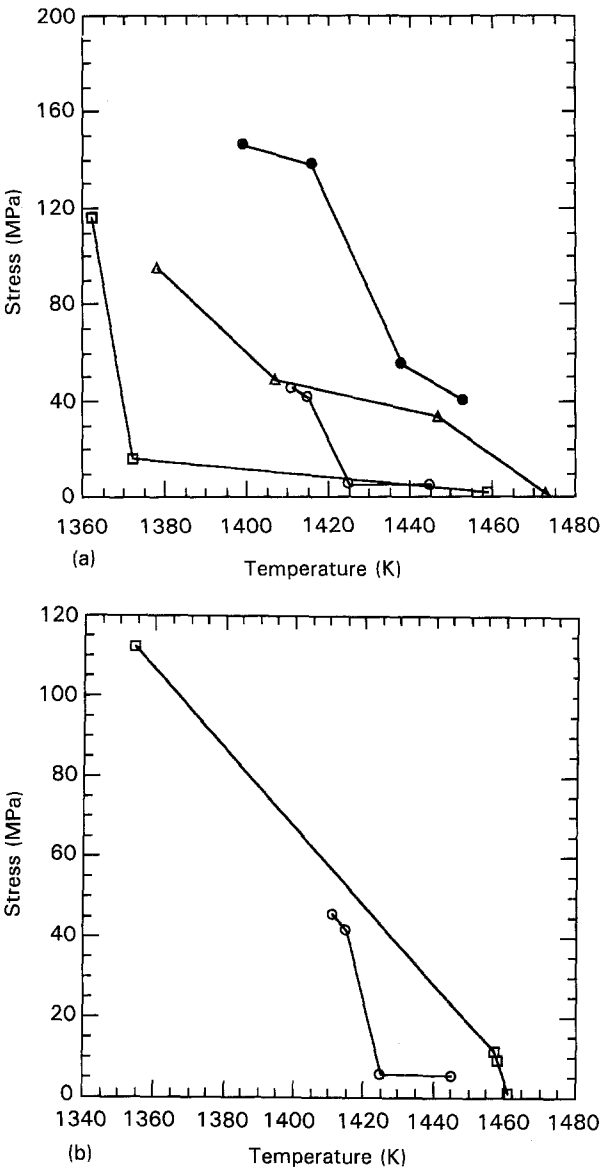

Figure 9 (a) The transverse engineering stress to failure versus temperature for the same temperature gradient, $G = 8.1\ K\,mm^{-1}$, for various velocities, $V = 4.7$, 37, 75 and 150 $\mu m\,s^{-1}$. (b) The transverse stress at failure versus temperature for directionally solidified Rene 108 at a velocity $V = 37.5\ \mu m\,s^{-1}$ and varying temperature gradient. (a) —⊟— $G = 8.1$ K mm, $V = 4.7$ μm s, —⊖— $G = 8.1$ K mm, $V = 37$ μm s, —△— $G = 8.1$ K mm, $V = 75$ μm s, —●— $G = 8.1$ K mm, $V = 150$ μm s, (b) —⊟— $G = 13.6$ K mm, $V = 37$ μm s, —⊖— $G = 8.1$ K mm, $V = 37$ μm s.

4.4. Fracture in directionally solidified alloys

The effect of the temperature gradient (G) and growth rate (V) on the fracture stress in the transverse direction (σ_T) is to increase the fracture stress (Fig. 9). The temperature at which the fracture stress becomes very small (i.e. total loss of coherency) is higher for the longitudinal section when compared to the transverse section. Additionally, it is noted that the solidification variables may influence this temperature significantly. This temperature is the upper hot-tearing temperature and is noted to be a function of the imposed solidification variables which control the morphology of growth. The upper hot-tearing temperature is obtained by extrapolating the σ_T–T curve to obtain the temperature at which $\sigma = 0$. The upper hot-tearing temperature increases with the temperature gradient, G, imposed during solidification (Fig. 10). The upper hot-tearing temperature is noted to be relatively insensitive to the solidification velocity in the range of (1–20 $\mu m\,s^{-1}$) but then increases in the range of 40–160 $\mu m\,s^{-1}$. The reason for the upper hot-tearing temperature being insensitive to the velocity in the range of low velocity is because of the cell morphology. As the solidification velocity increases the secondary arm spacing (λ_2) decreases in the Rene 108 alloy. For transverse testing this may imply higher frictional forces during deformation and an increase in the strength with increasing solidification velocity. Fig. 11 is a plot of the secondary arm spacing and transverse strength. A correlation is apparent which shows the transverse stress falling with increasing λ_2.

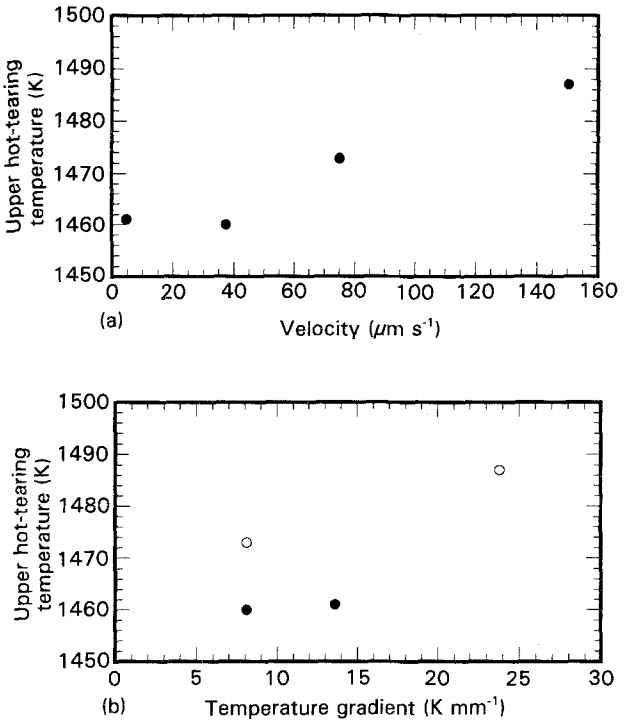

Figure 10 Upper hot tearing temperature (the temperature below which the alloys start to gain strength) as the function of (a) velocity and (b) temperature gradient for directionally solidified Rene 108. $G = 8.1\ K\ mm^{-1}$, (●) $37\ \mu m\ s^{-1}$, (○) $75\ \mu m\ s^{-1}$.

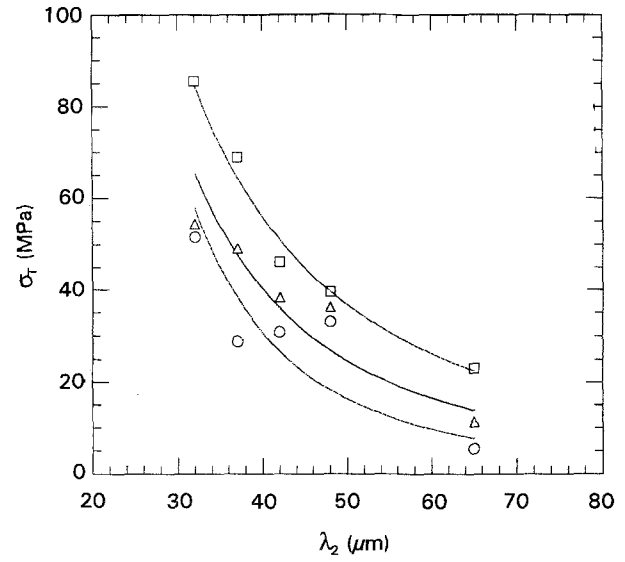

Figure 11 The fracture stress at a given temperature as a function of the secondary dendrite arm spacing (λ_2) for directionally solidified Rene 108. The best fit lines were obtained with an exponential fit.

4.5. Hot-tearing susceptibility

The hot-tearing resistance is related to the amount of strain accommodation that is possible, although alternative definitions are available when lower fraction solids are considered [2, 3, 17–19]. Smaller grain sizes in equiaxed castings are known to be more resistant to hot-tearing than the higher grain size [17–19].

For directionally solidified samples, a higher fracture strain is noted for longitudinal testing than for transverse testing. When comparing transverse tested samples which were solidified at the same velocity, but with different temperature gradients, it is noted that

TABLE VI The physical properties of Rene 108

Solidus temperature, T_S	1400 K
Liquidus temperature, T_L	1769 K [8]
Solute diffusivity in melt, D_L	$13.9 \times 10^{-9}\ m^2\ s^{-1}$ [8]
Liquid–solid surface energy, γ	$0.225\ J\ m^{-2}$ [8]
Solute partition coefficient, k	0.1 [8]
Entropy of melting, ΔS	$10^6\ J\ m^{-3}\ K^{-1}$ [8]
Freezing range, ΔT_0	369 K [8]

TABLE VII The transverse strain at maximum stress at different temperatures for directionally solidified Rene 108 for temperature gradient $G = 8.1\ K\ mm^{-1}$

Temperature (K)	Velocity ($\mu m\ s^{-1}$)			
	150	75	37	4.7
1400	0.049	0.034	0.037	0.02
1420	0.076	0.029	0.041	0.02
1440	0.053	0.022	0.007	0.01
1450	0.039	0.019	–	–

TABLE VIII The transverse strain at maximum stress at different temperatures for directionally solidified Rene 108 for velocities $V = 37$ and $75\ \mu m\ s^{-1}$

Temperature (K)	Temperature gradient ($K\ mm^{-1}$)	
	8.1	13.6
Velocity = 37 $\mu m\ s^{-1}$		
1400	0.037	0.024
1420	0.041	0.019
1440	0.007	0.012
1450	–	0.031
Velocity = 75 $\mu m\ s^{-1}$		
1400	0.034	0.043
1420	0.029	0.054
1440	0.022	0.039
1450	0.019	0.031

the fracture strain increases with increasing temperature gradient. This is true for high velocity in the high range, $75\ \mu m\ s^{-1}$. In the lower range of velocity the relationship is more complex. For the transverse samples in the same temperature gradient range a higher velocity gives a higher strain accommodation (see Tables VII and VIII). Thus, there are two controlling parameters, the morphology and the microsegregation, for determining strain accommodation. The morphology being more important when cells and two-fold dendrites are present.

It is noted that the upper hot-tearing temperature for DS transverse tested increases with V and G. This result agrees with previous results for nickel aluminide [3]. It is also noted that the hot-tearing stresses are generally also expected to increase with V and G. The fracture strain dependence on V, G is dependent on whether morphology control or microsegregation control dominates. For the transverse DS samples, broadly speaking, the increase in the coherency temperature will decrease strain accommodation for dendritic samples but will increase strain accommodation for two-fold or cellular samples.

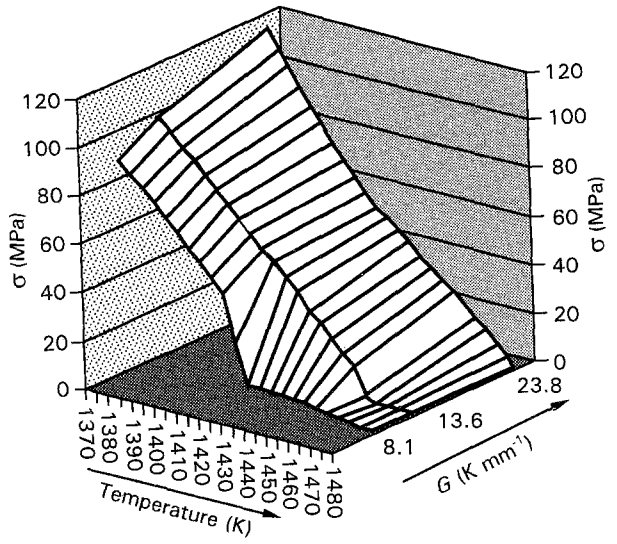

Figure 12 The 3D diagram fracture map (transverse stress at fracture-temperature-temperature gradient) at a fixed velocity of ca. 38 $\mu m\,s^{-1}$ for the directionally solidified Rene 108 alloy.

4.6. Fracture maps for the nickel-base superalloy Rene 108

Fracture maps may be defined as processing-property maps which may critically impact on casting design [2, 3]. These maps should reflect the conditions under which the casting will tear during processing. The fracture maps for Rene 108 have been developed after a critical examination of the solidified microstructure and the semi-solid strengths. The fracture maps are the T–σ_T–G (transverse) for the directionally solidified microstructure. The T–σ_T–G map is shown in Fig. 12. For a casting process information may be obtained on temperature gradient, G, during solidification. In addition, it is fairly simple to estimate the magnitude of mould-imposed stress on a casting [14, 20–22]. By comparing such values with the T–σ_T–G map a determination may be made if there is any value that lies above the net. If a problem is anticipated, parameters like mould design, temperature gradient, etc., may be changed to ascertain that there is no processing condition above the critical net.

4.7. Castability maps for the nickel-base superalloy Rene 108

The castability concept [23] and castability maps for multicomponent nickel aluminide [2, 3] were generated in previous studies. A similar analysis may be made for Rene 108. The ratio of imposed stress to the fracture stress at a given temperature as a function of velocity are plotted in Fig. 13. The thermal expansion coefficient, α, is taken to be $13.6 \times 10^{-6}\,K^{-1}$ for the alloy, σ_f is the fracture stress at a given temperature, T, and E_T is the measured modulus at the same temperature. The quantities σ_f and E_T are measured from plots such as Fig. 6. The amount of measured primary γ' varies with velocity. In previous studies [2, 3], it was noted that the volume fraction of γ' influenced the modulus, and thus the residual cracking found in castings after solidification. For the cell morphology (the low velocity region), the volume fraction of γ' is lower than the dendritic morphology. From Fig. 13

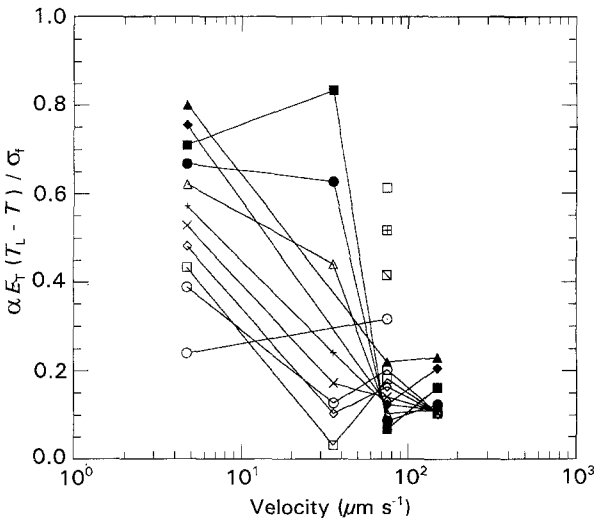

Figure 13 The ratio of imposed stress to the fracture stress at a given temperature versus velocity for directionally solidified Rene 108 at temperature gradient, $G = 8.1\ K\,mm^{-1}$. α is taken to be $13.6 \times 10^{-6}\,K^{-1}$ for the alloy, T; E_T is the measured modulus at a given temperature. T_L is the liquidus temperature. T is a given temperature. σ_f is the fracture stress at the same temperature. —○— 1410 K; —□— 1415 K; —◇— 1420 K; —×— 1425 K; —+— 1430 K; —△— 1435 K; —●— 1440 K; —■— 1445 K; —◆— 1450 K; —▲— 1455 K; —⊙— 1460 K; —▨— 1465 K; —⊞— 1470 K; —⊡— 1475 K.

a higher value for the ratio of imposed stress to the fracture stress at lower velocities is noted. From such a plot the processing conditions that give a higher value of the ratio can be identified and avoided. The microporosity value shown in Fig. 5a can be replotted as iso-microporosity lines, as shown in Fig. 14. From this plot it can be seen that at certain values of temper-

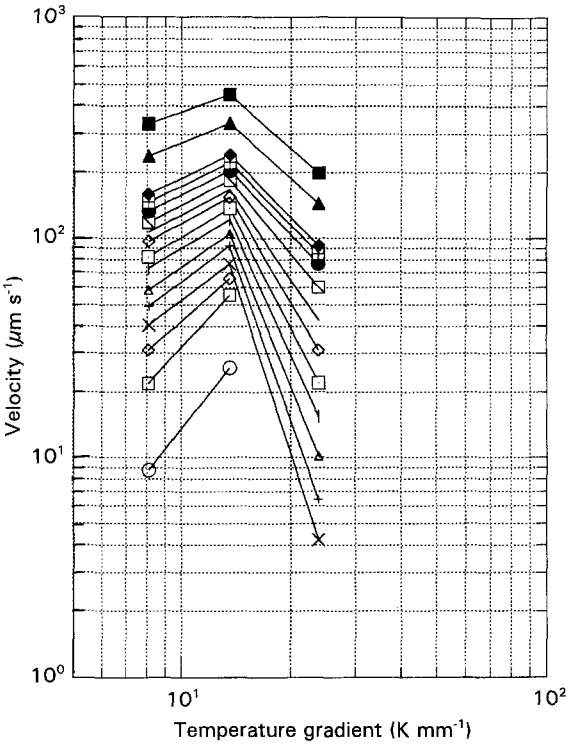

Figure 14 Iso-microporosity lines in the castability map of directionally solidified Rene 108. The number given along with the figure are the percentage of the microporosity. Such a map could be used as a design tool for determining the processing conditions. —○— 0.05%; —□— 0.08%; —◇— 0.09%; —×— 0.10%; — 0.11%; —△— 0.12%; —+— 0.13%; —⊡— 0.14%; —◇— 0.15%; — 0.16%; —▨— 0.17%; —●— 0.18%; —⊞— 0.19%; —◆— 0.20%; —▲— 0.25%; —■— 0.30%.

ature gradient the porosity is very sensitive to small changes in the velocity.

5. Conclusions

In the present investigation a nickel-base superalloy was directionally solidified under a range of growth rates with three different temperature gradients and its characteristic microstructural features were investigated. The primary and secondary dendrite arm spacing (λ_1 and λ_2, respectively) were measured as functions of the growth rate and the results compared to those anticipated from well-established theoretical models for dendritic growth. The semi-solid strength, ductility and the upper hot-tearing temperature were also measured, and shown to be functions of the temperature and the solidified microstructure morphology. The results may be summarized as follows:

1. The fracture strength in the semi-solid zone at any temperature below the upper hot-tearing temperature increases with temperature gradient and velocity. The fracture strain is dependent on V and G, and is also dependent on whether morphology control or microsegregation control dominates.
2. When considering processing maps for Rene 108, the temperature gradient during solidification and the transverse direction properties limit the processing and these are the important variables.
3. The ratio of the imposed stress to the fracture stress for the cell morphology is higher than for the dendritic morphology. The dendritic morphology has less hot tearing susceptibility than the cell.

The volume fraction of primary γ' and the microporosity depend on V and G. There is a critical temperature gradient where a small change in solidification velocity can strongly influence the amount of microporosity.

Acknowledgements

This work was performed as part of an Edison Material Technology project CT-17.

References

1. M. McLEAN, "Directionally solidified materials for high temperature service" (The Metal Society, London, 1983) p. 151.
2. C. S. LIN and J. A. SEKHAR, *J. Mater. Sci.* **28** (1993) 3581.
3. *Idem, ibid.*, **28** (1993) 3885.
4. C. T. HO, C. J. CHENG and J. A. SEKHAR, *Metall. Trans.* **22A** (1991) 225.
5. P. N. QUESTED and M. McLEAN, *Mater. Sci. Engng* **65** (1984) 171.
6. H. K. KIM, J. C. EARTHMAN and E. J. LAVERNIA, *Acta Metall.* **40** (1992) 637.
7. G. F. BOLLING and D. FAINSTEIN-PEDRAZA, *ibid.*, **22** (1992) 1033.
8. T. KELLY, "Thermophysical properties of liquid Rene 108", G.E. Report (1990).
9. W. KURZ and D. J. FISHER, *Acta Metall.* **29** (1981) 11.
10. R. TRIVEDI, *Metall. Trans.* **15A** (1984) 977.
11. H. ESAKA and W. KURZ, *J. Cryst. Growth* **72** (1985) 578.
12. M. H. BURDEN and J. D. HUNT, *ibid.*, **22** (1974) 99.
13. *Idem, ibid.*, **22** (1974) 109.
14. M. A. ESHEIMAN, V. SEETHARAMAN and R. TRIVEDI, *Acta Metall.* **36** (1988) 1165.
15. M. C. FLEMINGS, "Solidification processing" (McGraw-Hill, New York, 1974).
16. U. FEURER and R. WUNDERLIN, "Fachbericht der deutsche gesellschaft fur metallkunde" (Oberursel, FRG, 1977).
17. S. W. METZ and M. C. FLEMINGS, *AFS Trans.* **77** (1969) 329.
18. W. S. PELLINI, *Foundry* **8** (1952) 125.
19. M. KUBOTA and S. KITAOKA, *AFS Trans.* **81** (1973) 424.
20. A. ETIENNE and A. PALMERS, in "Solidification and casting of metal" (The Metals Society, London, 1979) p. 295.
21. A. GRILL, J. K. BRIMACOMBE and F. WEINBERG, *JISI* **211** (1976) 34.
22. J. MATHEW and H. D. BRODY, in "Solidification and casting of metal" (The Metals Society, London, 1979) p. 244.
23. J. A. SEKHAR, C. S. LIN and C. J. CHENG, in "Nature and properties of semi-solid materials", edited by J. A. Sekhar and J. Dantzig (The Minerals, Metals and Materials Society, 1991) p. 267.

Received 15 December 1993
and accepted 10 January 1994